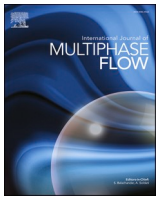
International Journal of Multiphase Flow 180 (2024) 104955



Contents lists available at ScienceDirect

International Journal of Multiphase Flow

journal homepage: www.elsevier.com/locate/ijmulflow



Review Article



On charging and breakup of paints using a high-speed rotary bell atomizer with internal charging system

Q. Ye [a,*], B. Shen [b], O. Tiedje [a], P. Knee [a], J. Domnick [b]

[a] Fraunhofer Institute for Manufacturing Engineering and Automation, Stuttgart, Germany
[b] University of Applied Sciences, Esslingen, Germany

ARTICLE INFO

Keywords:
Rotary bell atomizer
Electro-hydrodynamics
Charge migration
Liquid breakup

ABSTRACT

Experimental and numerical studies on charge transport and liquid atomization with the consideration of electrohydrodynamics (EHD) have been performed for a high-speed rotary bell atomizer with internal charging system. The VOF-to-DPM hybrid model in the commercial CFD code ANSYS Fluent is used to investigate and analyse the liquid breakup. Furthermore, the charge conservation equation is solved not only considering flow convection but also the significant ion drift convection due to the presence of the strong electric field. We introduce the so-called apparent ion mobility coefficient that depends on the permittivity and conductivity of liquid, the film thickness on the bell surface and the electric field strength. With this model we can calculate the charge migration from the electrode, in this case the bell surface, to the liquid film and the droplets. Simulation results show an inhomogeneous charge distribution perpendicular to the bell surface, namely charge accumulating mainly on the film surface. Breakup simulations are carried out using a Newtonian liquid and a real paint. The electric body forces have been included in the Navier-Stokes equations. Effects of EHD on the liquid breakup are analysed. The relationship of droplet charge to droplet diameter is obtained, from which the total current is predicted that compared well with experiments. Simulation results deliver useful information for an improved understanding of the relevant physical processes.

1. Introduction

Electrostatically supported high-speed rotary bells are widely used in high-quality organic coating applications. A high paint transfer efficiency can be achieved by applying high voltage directly to the rotating bell, which is the so-called direct or internal charging technique. It is well known that mainly the bell speed is the dominating factor for the atomization due to aerodynamic effects on the liquid breakup process. So far, effects of the electric field forces on the atomization process were neglected. Their contribution was limited to the movement of the charged droplets between atomizer and target.

Due to the underlying complex physical processes, research on the charge migration in a leaky dielectric liquid film and on the effects of electrohydrodynamics (EHD) on liquid breakup is very limited. In the past, most of the experimental and numerical investigations focused on the two-phase flow field between atomizer and target and the effects of process parameters on the final coating thickness on the target (Domnick et al., 2005; McCarthy and Senser, 2006; Mark et al., 2013; Stevenin et al., 2015; Chen et al., 2017; Guettler et al., 2020; Pendar and Páscoa, 2021). Thereby, most numerical simulations use measured droplet distributions as well as empirical charging laws for droplet charge to calculate the droplet trajectories in the two-phase flow field and the electric field. For instance, in analogy to the limiting droplet charges given by the Rayleigh-law (Rayleigh, 1882), (small) percentages of these maximum charges were used in simulations (Domnick et al., 2005; Guettler et al., 2020), depending on the material and the operating parameters. Other researchers (Mark et al., 2013) assumed that the droplet charge is proportional to the droplet surface.

There are some investigations of the atomization process of rotary bell atomizers (Thieme and Domnick, 2006; Oswald et al., 2018; Wilson et al., 2018; Shen et al., 2019). Newtonian (Thieme and Domnick, 2006) and non-Newtonian liquids (Oswald et al., 2018) were used for experimental studies of the breakup processes. Images of the liquid disintegration process at the bell edge were recorded by using a high-speed camera. Droplet velocity and size distributions in the near bell region and downstream in the spray cone were determined using Phase-Doppler-Anemometry (PDA). Numerical simulations of primary breakup of a non-Newtonian liquid using a high-speed rotary bell were

* Corresponding author.
E-mail address: qiaoyan.ye@ipa.fraunhofer.de (Q. Ye).

https://doi.org/10.1016/j.ijmultiphaseflow.2024.104955
Received 3 April 2024; Received in revised form 18 July 2024; Accepted 8 August 2024
Available online 10 August 2024
0301-9322/© 2024 Fraunhofer Institute for Manufacturing Engineering and Automation, Stuttgart, Germany,. Published by Elsevier Ltd. This is an open access article under the CC BY-NC-ND license (http://creativecommons.org/licenses/by-nc-nd/4.0/).

carried out (Shen et al., 2019), focusing on the film formation on the surface of the rotary bell and on the disintegration process of the paint liquid in the near-bell region, but without considering the film charging process and its effect on the disintegration process. Recently, a numerical study of a rotary bell atomizer including EHD effects was performed (Krisshna et al., 2023) using a high-fidelity volume-of-fluid transport scheme, in which a simplified cylinder model for the liquid jet emerging from the bell edge was applied due to the serrated bell geometry. By a given initial charge density in the liquid jet inlet plane, charge migration within liquid ligaments and to drops were calculated and the effects of electric field on the liquid breakup were analysed.

There are some numerical studies of EHD atomization, however mainly for the cone-jet type disintegration (Hartman et al., 1999; Lastow and Balachandran, 2006; Ouedraogo et al., 2021), where a liquid is supplied to a pressure nozzle at low flow rate and at low voltage. The shape of the liquid cone and jet, the electric fields in and outside the cone, the surface charge density at the liquid surface, and droplet formation were calculated. Ouedraogo et al. (2021) found that the charge of primary electrospray droplets is directly proportional to their volume and this charge-radium correlation is independent from the applied liquid flow rate.

Kourmatzis and Shrimpton (2009) provided an overview of the governing equations of the EHD process concerning dielectric liquid atomization, focusing on the understanding of the application of the basic equations to the atomizer internal flow. Relevant time scales were proposed and discussed to understand the dominant mechanism for charge transport in charge injection atomization. Similar hydrodynamic and electrostatic governing equations and the time scales analysis were applied to consider multiphase EHD flows of a charged liquid kerosene jet (van Poppel et al., 2010).

Concerning the charge conservation equation, there are three mechanisms of charge transport: convection due to liquid velocity, drift by electric field and diffusion. The last one could be neglected compared to the other two (Castellanos, 1998). For complex processes of EHD convection, namely high liquid velocity, high electric field and strong charge density gradient, high-fidelity numerical simulations should be able to provide some assistance in answering questions about the fundamentals and dynamics of EHD atomization. To numerically determine the electro convection, liquid ion mobility must be provided. However, there are only a few reports about the sensitivity of the ion mobility coefficient on the final results of charge migration in liquids. In fact, it is quite difficult to determine ion mobility coefficient of leaky dielectric liquids (Bandara and Mellander, 2011). The ion mobility is defined as $\mu_{ion} = v/E$, where v is the ion drift velocity and E the electric field. Clark et al. (2019) investigated the effect of an external electric field on the ion movement in an ionic liquid. They reported that there is a non-linear correlation between ion drift velocity and electric field, leading to variations of μ_{ion} as a function of the electric field strength also. The dependence between liquid viscosity and ion mobility was reported in (Gzowski, 1962).

For the modelling of gas-particle two-phase flows, usually Eulerian-Lagrangian RANS (Reynolds-averaged Navier-Stokes) methods are used, especially for industrial applications because of the lower computational cost. However, with the availability of high-performance computational capabilities and the improvement of numerical schemes the LES (large-eddy-simulation) - Lagrangian approach becomes more and more attractive and has been used also in the spray painting simulation (Pendar and Páscoa, 2021). For swirling gas-particle flows, a comparison of LES – Lagrangian and RANS-Lagrangian was carried out (Zhou, 2023) indicating a superior performance of LES with respect to the axial and tangential velocity distributions. Due to the existing complexity of the physical problem and the required spatial resolution, RANS methods have been applied so far, but LES based simulations are planned in near future.

This paper deals with the film charging process on a high-speed rotary bell with internal charging. The unipolar injection of ions from the bell surface to thin leaky dielectric liquid film flowing on the bell surface and the resulting final droplet charges near the bell edge directly after liquid disintegration are studied. Experiments and numerical simulations of atomization with the consideration of EHD effects are carried out. The VOF-to-DPM hybrid model in the commercial CFD code ANSYS Fluent is used to investigate and analyse the liquid breakup. Based on extended user defined scalars and functions, the charge distribution in the film and in the droplets are calculated. Effects of liquid EHD properties and electric field strength on charging behaviours are investigated.

The paper will be organized as follows: In Section 2, we describe the experimental setup, the applied measuring techniques and some of our experimental results, namely the effect of the operating conditions on the total current. The obtained experimental results are essential for both the model development and the validation of the simulations results. In Section 3, the governing equations are developed and explained. For solving the charge conservation equation, we introduce a model for a so-called apparent ion mobility. The model constant related to the applied liquid is determined by the measured currents. Section 4 is devoted to the numerical methods, in which grid resolution and important boundary conditions are described. Two kinds of liquids, namely, a Newtonian liquid and a real paint liquid with significant difference of EHD properties are applied. In the section of results, we present and discuss the charge density distribution in the film and in the ligaments and the droplet charge distribution as well as the total current to the earthed target. Here, some comparisons between experiment and simulation are carried out. Based on the simulation results, we can explain some experimental results that are originally difficult to understand, concerning the effects of EHD. In the last section we summarized the important results.

2. Experimental investigations

The experimental investigations presented were carried out with an internal charging high-speed rotary bell ECOBELL 2 (Dürr Systems AG) with a 65 mm diameter unserrated bell edge, mainly used for high-quality automotive paint applications. Fig. 1 shows a photograph of the front part of the atomizer body and the rotating bell. Fig. 2 contains a cross section of the bell. Paint is supplied through a central nozzle at relatively low speed flowing towards the so-called distributor disk. Here, the liquid is distributed into a primary part forming a radially flowing film on the backside of the distributor disk and a secondary part, flowing through an auxiliary bore in the distributor disk and forming a film on

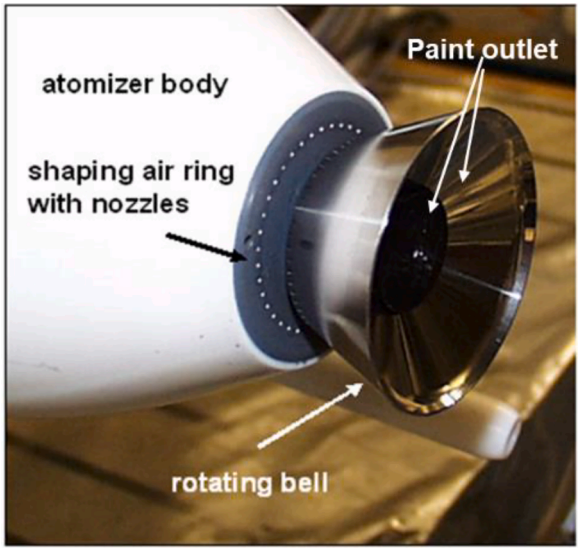


Fig. 1. Photograph of the used rotary bell atomizer.

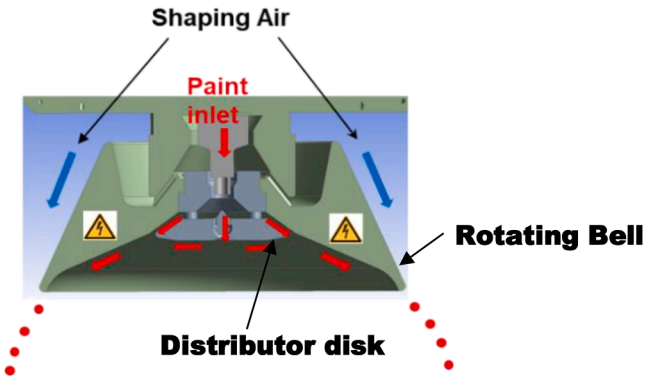


Fig. 2. Cross section of the bell (red: paint flow direction).

the front side. At the outer edge of the distributor disk both paint films detach from the distributor disk, finally forming a smooth paint film that propagates on the inner surface of the bell towards the bell edge (Shen et al., 2019). At the bell edge, the film disintegrates into ligaments and finally into droplets.

To direct these droplets axially towards the target, a so-called shaping air is flowing along the outer surface of the bell (see Figs. 1 and 2). In the considered atomizer construction, this air flow is emerging at sonic velocity from one ring of air nozzles which are oriented parallel to the bell axial direction.

In the case of internal charging atomizers, high voltage up to 80 kV is applied directly to the bell to initiate liquid charging during the film propagation on the bell surface, i.e., before the final disintegration process. Hence, charged droplets are formed resulting in electric forces that additionally direct the droplets towards the grounded target.

The investigated operating conditions of the atomizer, including also the very important working distance (bell edge to grounded target) are summarized in Table 1. The chosen conditions are all within the standard ranges used in automotive painting processes.

A Newtonian liquid, Butyl-acetate with 2 % of a conductivity agent (short name: Ba2per), whose electric properties are similar to a solvent borne paint, and a real water-based paint with a solid content of 18.5% used in automated painting processes were applied. The shear thinning viscosity behaviour of this paint was studied (Shen et al., 2019) and the resulting viscosity model is used in the present study. Liquid conductivity was measured using a DCA Electrospray Paint Resistivity Meter, the permittivity using an Alpha TDR-5000 Dielectric Constant Meter.

Due to the existing sensitivity on the final application results, namely the paint film thickness and the paint film appearance, the atomizer operation parameters are precisely controlled and kept stable. The final uncertainty of the parameters given in Table 1 is typically less than ±1 % of the actual value. Throughout all experimental investigations, the atomizer was mounted on a dedicated 6-axis painting robot to ensure a precise control of the atomizer movement, orientation, and position. Its point-related precision is verified to better than ± 1 mm.

For detailed investigations of the spray properties (local droplet size, velocity, and flux) a DANTEC phase-Doppler system has been used, consisting of an ArIon gas laser, a 2-component fibre probe and a 112 mm fibre-based receiver, both optics equipped with 500 mm lenses (Fig. 3). At a scattering angle of 72°, which was appropriate for all investigated fluids to obtain 1st order refracted scattered light, the maximum droplet size was around 130 μm. The light power in the probe volume was typically around 30 mW per beam. This setup was chosen as a compromise between the desired maximum spatial resolution and the need to perform measurements at voltages up to 60 kV. Up to 16 measurements with a point-to-point distance of 10 mm were performed at 50 mm and 100 mm axial distances from the bell edge plane. At each measurement location, the measurement duration was limited to either 5000 validated samples or 5 s. Due to the presence of high voltage the optical fibre connections were completely manufactured from non-conductive materials.

For further comparisons with numerical results, global spray characteristics must be derived from the pointwise results of the PDA measurements. Therefore, local results, e. g. local mean diameters, have been integrated using a number flux and area weighting procedure. Fortunately, the present spray cones are perfectly axial symmetric; therefore, the area weighting reduces to a simple integration of annular rings with increasing radius. The corresponding equation is given as (2.1). Here, we use only the volume weighted mean D_{30},

$$\overline{D_{30}} = \frac{\sum_{i=1}^{n} D_{30,i}\, \dot{n}_i\, A_i}{\sum_{i=1}^{n} \dot{n}_i\, A_{tot}}, \tag{2.1}$$

where $A_i = 2\pi r_i \Delta r$.

Only for experiments without high voltage, a Malvern Spraytec particle sizer could be applied additionally to the PDA, yielding a 400 μm particle size range with a 200 mm receiving lens. The axis of the measuring volume of the Spraytec, having a diameter of 9 mm, was positioned at approximately 10 mm from the bell edge to be able to detect the true droplet production of the atomizer. This is of specific importance as Fraunhofer diffraction instruments measure a concentration weighted size distribution that is affected by the presence of size/velocity correlations. On the other hand, the visualizations indicate the formation of the final droplet size distribution at this position.

It should be stressed that it is not possible to directly compare PDA and diffraction results, neither droplet size distributions nor mean droplet diameters. This is not only because of the different measurement characteristics of both instruments (PDA: pointwise with flux weighting, diffraction: integral with concentration weighting), but also due to a decreasing sensitivity of the PDA technique at droplets below approx. 5 μm and the thereby reduced accuracy. In case of absent potential, Fraunhofer diffraction results are used to compare measured and

Table 1
Atomizer characteristics (sl: Standard litre).

Operation parameter	Dimension	Experimental range	Numerically investigated
Bell diameter (no serrations) D	mm	65	65
Bell speed n	1/min	25 000 – 60 000	40 000
Electric potential U	kV	0 – 80	0/30/60/80
Target distance L	mm	100 – 300	150
Liquid flow rate LF	ml/min	100 – 600	200 – 400
Shaping air flow rate SA	sl/min	50 – 300	50/180

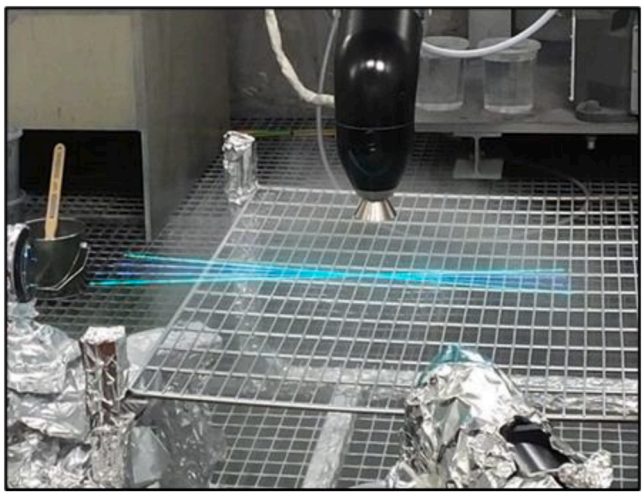


Fig. 3. PDA-Setup with a scattering angle of 72°.

simulated droplet size distributions. In addition, these measurements also indicating a significant fraction of droplets below 5 μm that will not be reliably detected by a PDA system. Therefore, the comparison between measurements and simulation in cases with applied potential, where only PDA could be applied, is limited to the volume weighted mean diameter D_{30}, which is less sensitive to a potential loss of small droplets.

Qualitative visualizations of the liquid disintegration process directly at the bell edge were performed by using a high-speed camera (Photron FASTCAM) and a specific macroscopic lens system. The image area was kept constant at typically 5×5 mm^2. Since an increasing frame rate is accompanied by a reduction of the image resolution, the frame exposure time was externally controlled by a 200 ns flashlight.

In Fig. 4, the experimental setup for the global earth current measurements is shown. It consists basically of a mesh-type target isolated from ground, equipped with an appropriate termination and a digital oscilloscope to store the time dependent current with high accuracy. The porosity of the mesh was chosen as a compromise between minimum impacts on the air flow, and, hence, on the overall spray propagation, and maximum transfer efficiency. The transfer efficiency was assumed to be higher than 98 % with mostly very small droplets missing the wire mesh. The whole setup was located in a large spray booth delivering a constant downdraft air velocity of 0.34 m s^{-1}. The standard deviation of the current measurements, also including experiments on different days, was found to be better than ±2 % of the actual value, indicating a very good measurement repeatability and stability of the setup and the conditions inside the spray booth.

In Fig. 5, results obtained at a high voltage setting of 60 kV, a liquid flow rate of 200 ml/min (Ba2per) and a target distance of 200 mm are visualized. The green line denotes the magnitude of the total current, directly obtained at the high voltage generator outlet. There is a constant difference between the values of the current delivered by the HV generator and the obtained earth current (magenta line), indicating certain current leakages mainly due to atomizer internal currents. It should be noted that the atomizer itself is mechanically mounted to a grounded robot arm. These leakages are well known and are the reason why the total liquid charging cannot be directly derived from the HV generator current. Interestingly, the current decreases immediately and significantly with paint flow rate trigger. In the presented case, the earth current is 13.62 μA.

In Fig. 6, the influence of the most important application parameters, i.e. applied voltage, target distance, liquid flow rate and bell speed on the earth current are summarized in the case of Ba2per. As expected, the current increases with increasing voltage and decreasing target distance, which is basically the effect of the increasing electric field strength between bell and target which is roughly proportional to U/L.

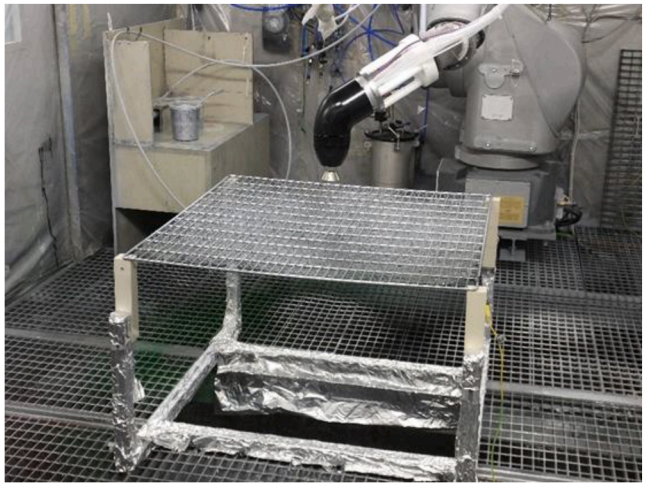


Fig. 4. Experimental arrangement for current measurements.

However, the influence of both paint flow rate and bell speed does not meet the expectations. Changing the liquid flow rate from 100 to 600 ml/min only a slight increase of the current can be observed, resulting in a significant reduction of the charge/mass ratio at higher flow rates. Also, the obtained influence of increasing bell speed, which leads to a reduction of the mean droplet diameters (Thieme and Domnick, 2006) of the spray and thereby to an increase of the droplet number flux and the available total droplet surface, indicates a target current decrease. Consequently, the mean charge on each droplet has also decreased. It will be shown and discussed below, that the liquid charging is mainly depending on the available free surface of the liquid film during its flow over the bell surface. Preliminarily, this surface is not affected by neither the liquid flow rate nor the bell speed.

3. Governing equations

For the numerical study of EHD atomization, coupled equations are applied for the transient electrostatic and fluid flow problem. Eqs. (3.1) and (3.2) are the Navier-Stokes equations. The last two terms in Eq. (3.1) denote the surface tension force density acting at the interface between the different fluids and the electric force density, respectively.

$$\frac{\partial \rho \boldsymbol{u}}{\partial t} + \boldsymbol{u}\cdot\nabla(\rho \boldsymbol{u}) = -\nabla \mathrm{p} + \rho \boldsymbol{g} + \mu\nabla\cdot\left(\nabla \boldsymbol{u} + \nabla \boldsymbol{u}^{T}\right) + \boldsymbol{f}_{s} + \boldsymbol{f}_{e} \tag{3.1}$$

$$\nabla\cdot\boldsymbol{u} = 0 \tag{3.2}$$

The electric potential φ can be calculated by Gauss's law, where ε is the permittivity, $\epsilon = \epsilon_0\epsilon_r$, ϵ_0 is the absolute permittivity, i.e. 8.85×10^{-12} $\frac{C}{mV}$ and ϵ_r the relative permittivity of the fluid. At the interface of the two-phase mixture, a mean value of the permittivity is used.

$$-\nabla\cdot(\varepsilon\nabla\varphi) = q \tag{3.3}$$

q is the space charge density that will be discussed later. The total electric force density applied on the fluid in (3.1) can be obtained from the divergence of the Maxwell stress tensor as (Castellanos, 1998)

$$\boldsymbol{f}_{e} = q\boldsymbol{E} - \frac{1}{2}E^{2}\nabla\epsilon + \frac{1}{2}\nabla\left(E^{2}\rho\frac{\partial\epsilon}{\partial\rho}\right), \tag{3.4}$$

where the electric field is given by (3.5)

$$\boldsymbol{E} = -\nabla\varphi \tag{3.5}$$

The Eq. (3.4) consists of three terms: the Coulomb force term, the dielectric force term and the force due to electrostriction. The second term is related to the local inhomogeneity and cannot be neglected for a two-phase flow, especially at the interface between gas and liquid. An estimation of the magnitude of electrostriction force was given by Liu et al. (2020). Considering the electrostriction force is much smaller than the other two forces, we neglect the contribution of the electrostriction to the total electric force.

For EHD flows one needs to solve the charge conservation equation. In this paper an effective unipolar charge in isotherm liquid, i.e. for simplicity a positive ion, is considered. The charge conservation equation for the charge density q in leaky dielectric medium can be written as (Melcher, 1981; Castellanos, 1998)

$$\frac{\partial q}{\partial t} + \nabla\cdot\boldsymbol{j} = 0, \tag{3.6}$$

$$\boldsymbol{j} = k\boldsymbol{E}q + \boldsymbol{u}q - D_{l}\nabla q, \tag{3.7}$$

$$\frac{\partial q}{\partial t} + \boldsymbol{u}\cdot\nabla q + k\mathbf{E}\cdot\nabla q = -k\frac{q^{2}}{\varepsilon} + D_{l}\nabla^{2}q, \tag{3.8}$$

where $\boldsymbol{j}$, k and D_l are current density, ion mobility and diffusion coefficient in the liquid, respectively. The second and the third terms on the

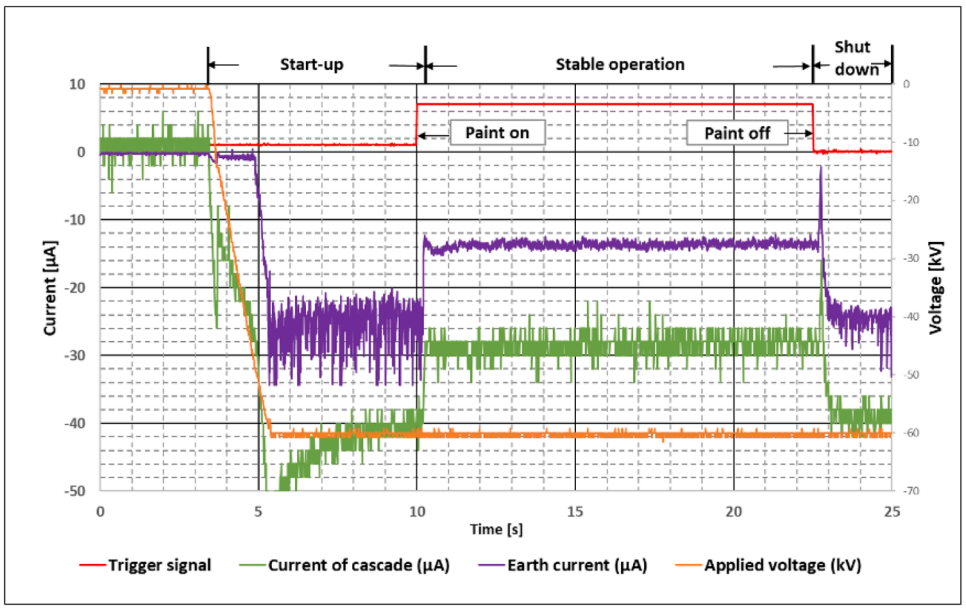


Fig. 5. Observed time dependent currents during on/off operation at 60 kV (Ba2per).

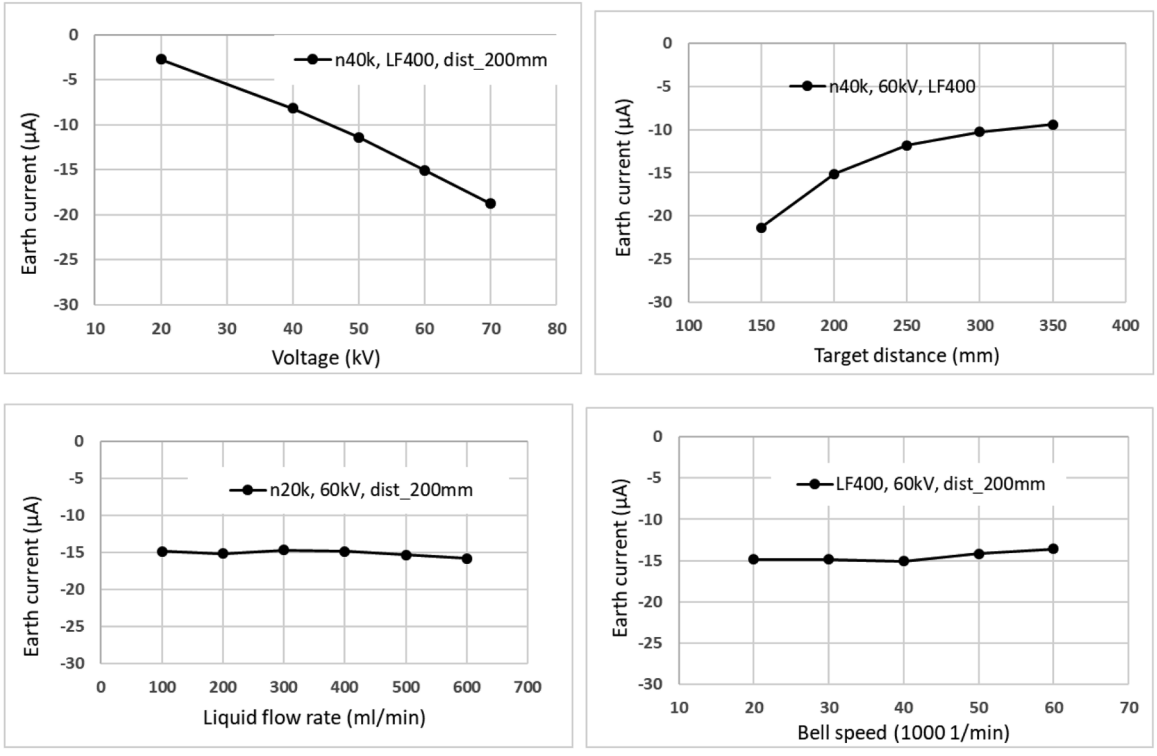


Fig. 6. Influence of application parameters on earth current (Ba2per).

left side of (3.8) are convection terms because of liquid flow velocity and the ion drift. The latter depends on the electric field and makes a significant contribution to the charge transport in case of very high electric field strength as in the present application. In some EHD applications (Aramide et al., 2019; Ouedraogo et al., 2021) the current density is described as $\boldsymbol{j} = \sigma \boldsymbol{E}$, where σ $\frac{1}{m\Omega}$ is the electric conductivity of the liquid that can be easily measured. Consequently, however, the electro-convection term disappears in the charge conservation Eq. (3.8), which might be suitable for cases with low electric fields, e.g. the Ohmic regime, but not for strong electric fields in dielectric media. The first and the second terms on the right side of (3.8) are called source term and diffusion term. The source term and the convection term play an important role for the charge generation and transport, the diffusion term is often neglected. In this study the charge diffusivity is considered.

Although the conservation equations for EHD flow are clearly defined, it is difficult to solve the charge conservation Eq. (3.8). The ion mobility is not easy to determine and is depends on the electric field (Clark et al., 2019). From the experimental point of view, it is easy to measure the electrical conductivity of liquid σ, but at a quite low electric potential. To estimate the ion mobility for the present application with

the high electric voltage, we introduce here an apparent ion mobility k^* by considering the definition $\sigma = kq$, and the Gauss's law $q = \varepsilon\nabla\cdot E$:

$$k^* = \frac{\sigma}{q} = f\left(\varepsilon, \sigma, E, \delta_{film}\right) = C\frac{\sigma\,\delta_{film}}{\varepsilon E}, \tag{3.9}$$

where σ and ε depend on the liquid EHD properties. The film thickness δ_{film} and electric field strength E on the bell result from the operating conditions. C is the model constant that is fitted from the measured current for a given liquid. Detailed results will be summarised in following sections. The corresponding ion diffusivity can be estimated (Bandara and Mellander, 2011) using the Nernst-Einstein relation,

$$D_l = \frac{k^*\,k_B\,T}{e}, \tag{3.10}$$

where k_B is the Boltzmann constant, T is the absolute temperature and e is the electronic charge of a particle.

After breakup of the liquid, the droplet trajectory can be calculated using the particle motion Eq. (3.11) based on the Lagrangian approach.

$$m_p\frac{\partial \boldsymbol{u}_p}{\partial t} = m_p\frac{\boldsymbol{u}-\boldsymbol{u}_p}{\tau_r} + m_p\frac{\boldsymbol{g}\left(\rho_p-\rho\right)}{\rho_p} + \boldsymbol{F}_E \tag{3.11}$$

The first term on the right side of (3.11) is the drag force, and τ_r is the droplet relaxation time that is a function of the droplet diameter, the viscosity of gas and the relative Reynolds number (Crowe et al., 2011). The second term is the gravity force. $\boldsymbol{F}_E = q_p\boldsymbol{E}$ is the electric force acting on a droplet, and q_p is the charge on the droplet that is obtained from the solution of the charge conservation equation and the breakup model. m_p, ρ_p and ρ are droplet mass, droplet density and air density, respectively.

One fundamental assumption in the classic dielectric model is that the electric charge introduced into a dielectric liquid has sufficient time to fully relax from a bulk volumetric charge to a surface charge. For the present application, it is necessary to estimate the relevant time scales in order to understand the dominant mechanism for the transport of the space charge. Following the work of (Kourmatzis and Shrimpton, 2009; van Poppel et al., 2010; Krisshna et al., 2023), the space charge relaxation time τ_{sc} that represents the typical time for a volumetric charge q to decay, and the flow advection time scale τ_f characterised for a fluid element to move a relevant length scale l_0 are described by

$$\tau_{sc} = \frac{\epsilon}{k^* q}, \tag{3.12}$$

$$\tau_f = \frac{l_0}{u} \tag{3.13}$$

The electric Reynolds number Re_e, is defined as the ratio of a charge relaxation time to the advection time,

$$\mathrm{Re}_e = \frac{\tau_{sc}}{\tau_f}\ . \tag{3.14}$$

In the following these time constants are estimated. For the advection time, it should be distinguished between the flow on the bell surface and the disintegration process. For the bell flow, the curvature radius of the bell edge, which is around 0.5 mm, is used as the relevant length scale l_0. With a relative film velocity on the bell surface of 2 m s^{-1} the resulting τ_f is 250 μs. Subsequently, the liquid film detaches from the bell surface at the sharp bell edge and forms ligaments, which are further accelerated by the effect of centrifugal forces. Measurements indicate a radial velocity of the detaching ligaments around 20 m s^{-1}. At a typical diameter of the ligaments of 50 μm, the resulting time scale τ_f is 2.5 μs.

For a typical paint liquid, the electric permittivity ε is 5.8×10^{-10} F/m. Assuming a mean volumetric charge q of 7.5 C/m^3 and an apparent ion mobility of 2×10^{-5} m^2/V/s, the space charge relaxation time τ_{sc} is 3.8 μs. Hence, the corresponding electric Reynolds number Re_e varies between 0.015 and 1.5. As these two time scales especially in disintegration region are in the same order of magnitude, it is necessary to model the charge transport considering both convection terms in Eq. (3.8).

In addition to the two time scales derived above, that were often used for the analysis of EHD problems, an ionic transit time that is defined as the time taken for a fluid element to move a distance δ due to electric convection was given by (Kourmatzis and Shrimpton, 2009). Here, we use the film thickness on bell as the relevant scale δ, which is approximately 20 μm for the paint liquid at a flow rate of 400 ml/min.

$$\tau_k = \frac{\delta}{v} = \frac{\delta}{k^* E} = \frac{\delta^2}{k^* U}, \tag{3.15}$$

in which the ion drift velocity v is used. The ionic transit time τ_k for our application is about 3×10^{-4} μs at an electric potential of 60 kV, which is quite small in the present application because of the thin liquid film on the bell.

4. Numerical methods

The numerical simulations were carried out using the commercial CFD code ANSYS Fluent based on the finite volume approach. A high-speed rotary bell (ECOBELL 2) as described in Section 2 with a smooth bell edge was investigated. Due to the given rotational symmetry of the spray cone and the limitation of the computational capacity, only a small segment of the bell with an extension of 3° was considered, as shown in Fig. 7. For the gas phase, the three-dimensional compressible airflow was calculated using a segregated solver. The turbulent transport was modelled using the sst k-ω model.

The shaping air is flowing through the upper surface into the computational domain (air inlet in Fig. 7). The 3 dimensional inlet conditions at this surface were obtained through detailed shaping airflow simulations (Shen et al., 2019). For the film inlet both liquid mass flow rate and film thickness should be given. For Newtonian liquids, the film thickness on the bell can be estimated (Hinze et al., 1950; Bayvel and Orzechowski, 2018) according to the following equation

$$\delta = \left(\frac{3\nu_L Q}{2\pi r^2\omega^2\sin\beta}\right)^{\frac{1}{3}}, \tag{3.16}$$

where Q, ν_L, ω, r, β are the liquid volume flow rate, the kinematic viscosity, the angular velocity of the bell, the radius of the position and the contour angle of the rotary bell cup, respectively.

For non-Newtonian liquids, where the viscosity is a function of the local shear rate $\dot{\gamma}$, this equation is not applicable. However, the dynamic viscosity of non-Newtonian fluids can be represented by a simple exponential function,

$$\eta = k_1\cdot\dot{\gamma}^{k_2}, \tag{3.17}$$

where k_1 and k_2 are dimensionless constants that can be determined through viscosity measurements. For the paint used in our investigations k_1 and k_2 are 0.3804 and -0.232, respectively.

From the momentum balance, the shear stress can be written as

$$\tau = \rho r\omega^2 y\sin\beta, \tag{3.18}$$

where y is the direction normal to the wall surface and perpendicular to the direction of the liquid flow. A generalized form of Newton's law of viscosity is written as

$$\tau = \eta\cdot\dot{\gamma} \tag{3.19}$$

From the above three equations, the liquid volume flow rate can be derived as

$$Q = 2\pi r C_0\cdot\frac{k_2+1}{2k_2+3}\cdot\delta^{\frac{2k_2+3}{k_2+1}} \text{ with } C_0 = \left(\frac{\rho r\omega^2\sin\beta}{k_1}\right)^{\frac{1}{k_2+1}} \tag{3.20}$$

Using this equation, the liquid film thickness δ for the paint on the

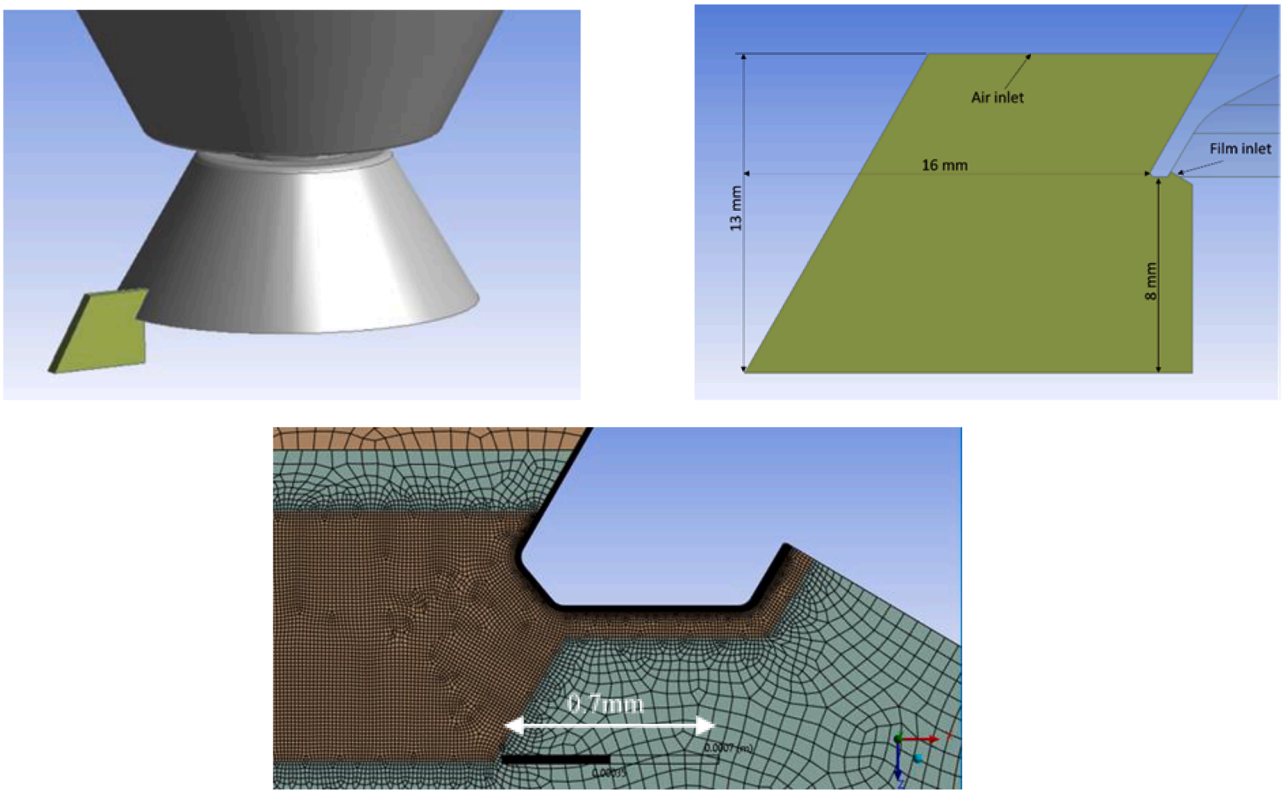


Fig. 7. Geometry model and computational mesh used in the breakup simulations.

bell surface can be determined as a function of the flow rate.

The necessary potential profiles on the lower surface of the domain (towards the target) and on the radial air inlet plane were obtained from additional simulations with a complete bell by solving the Laplace potential with a painting distance of 150 mm between the bell edge and the earthed target. In addition, on the bell wall the electric potential and the zero gradient of charge density were applied. All simulations were performed with moving wall boundary conditions according to the given bell speed.

Fig. 7 shows the meshed computational domain with the hex-grid. It should be noted that the exact shape of the bell edge as it is used in the simulations is directly taken from measurements using a 3D digital microscope. The domain is sliced into several parts with different mesh resolutions. The region near the bottom edge of the bell, where the primary breakup occurs, was meshed with a grid size of 5×5×5 μm. The bell mesh size is about 2×2×2 μm. 20 Prism layers were created on the surface of the bell with a constant distance of 2 μm, which provides the necessary resolution for the calculation of the film thickness on the bell. A coarser grid was applied in the remaining domain since it is not necessary to carry out two-phase flow calculations in these regions. The total cell number is about 17 million.

Electric potential (3.3) and charge conservation (3.8) were solved by using user-defined scalar transport equations implemented in ANSYS Fluent. The Volume-of-Fluid (VOF) model with Geo-Reconstruct discretization scheme was used to calculate the two-phase field and the gas-liquid interface. For time dependent VOF calculations, variable time stepping was used to account for interfaces moving through dense cells or high interface velocities. As a result, the time steps varied between 0.01 and 0.1 μs based on the preconfigured maximum global Courant number of 1, which ensures the computational stability of the numerical simulations. For breakup simulations, we applied the VOF-to-DPM (Volume of Fluid – Discrete Phase Model) available in ANSYS Fluent, to transfer non-spherical VOF lumps into DPM droplets. Since the charge density in the liquid film is not homogeneously distributed, a user-defined code was developed to detect the charge of each individual droplet. By collecting the droplets at a certain distance from the bell edge, the total current due to the charged droplets can be estimated. The interaction of droplets and the air flow was taken into account. In the present numerical simulations, we consider only the primary breakup of liquids. Models for secondary breakup and droplet collision are not taken into account.

5. Results and discussion

5.1. Breakup simulations without electric field

As a first step, simulations were carried out without electric potential by using the Newtonian liquid Ba2per. The corresponding operation conditions and liquid properties are listed in Tables 1 and 2. Figs. 8 and 9 show the breakup results quite close the bell edge as top view and front view. In general, the liquid does not detach from the bottom edge of the bell surface as expected. Instead, it flows around this first edge and further along the outer surface to a 2nd edge on the inclined bell surface, where the final detachment of the film and its disintegration into ligaments and droplets occurs. Parts of the film and large ligaments that might still undergo a further disintegration are coloured in magenta. At 1 mm from the bell edge, it was found that the disintegration process is finished. The simulation results correctly indicate the formation of ligaments close to the bell edge (Fig. 8, a), however, the calculated lengths

Table 2
Properties of the applied fluids.

Fluid property	Dimension	Ba2per	Water-based paint
Density	kg m^{-13}	880	1020
Viscosity	Pa·s	0.0007	Shear thinning
Surface tension	N/m	0.030	0.024
Relative permittivity	*(-)*	1.7	65
Electric conductivity	*S* m^{-1}	2.165×10^{-5}	$\sim7.5\times10^{-5}$

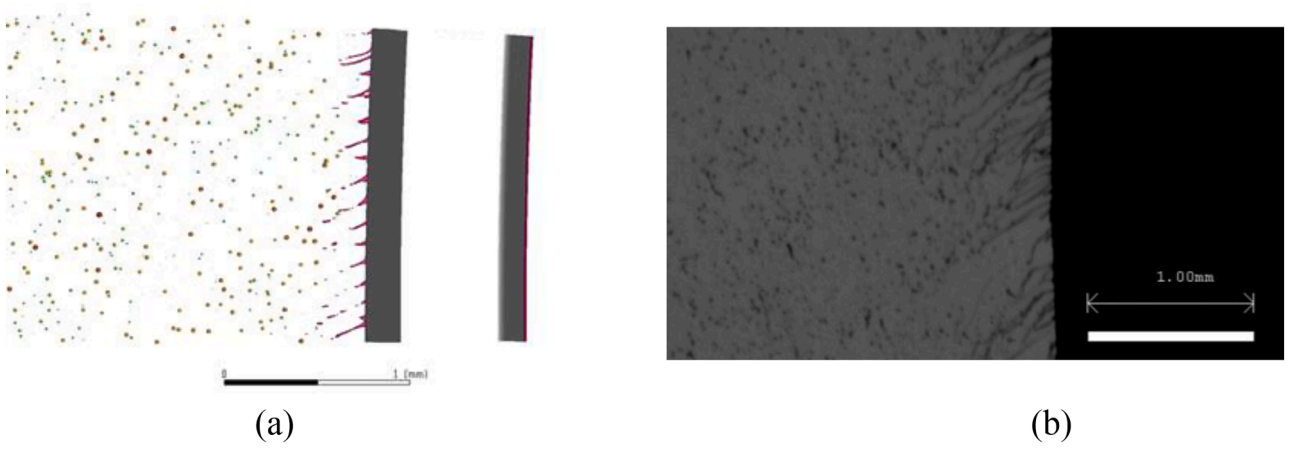


Fig. 8. Breakup simulation top view (a) vs. experiment (b), colours in the simulation depict the droplet size, magenta is not fully disintegrated.

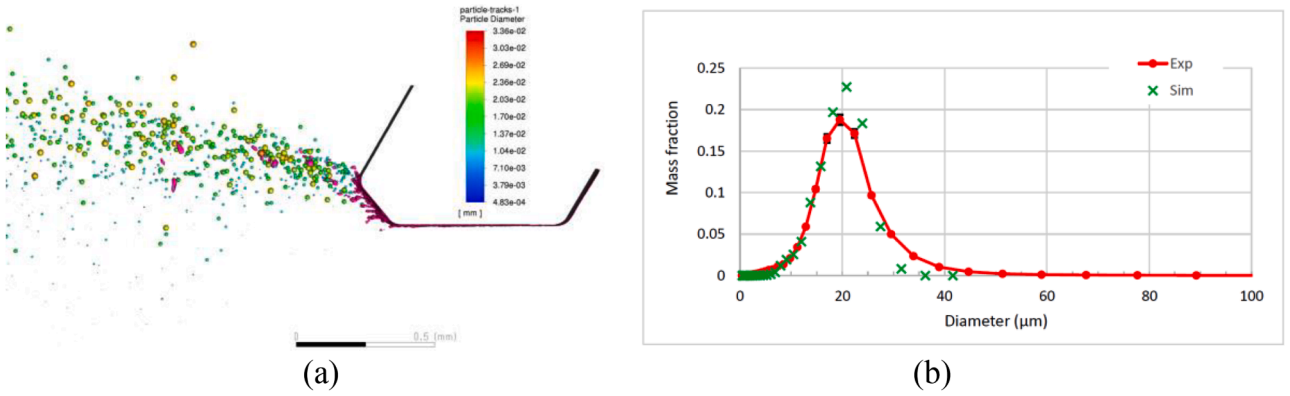


Fig. 9. Breakup simulation at a bell speed of 40 000 1/min and a liquid flow rate 200 ml/min: front view (a) and droplet size distribution (b), colours in the simulation depict the droplet size, and magenta is not fully disintegrated.

of these ligaments are shorter than those from the experimental observations (Fig. 8, b).

In the simulations, the droplets were collected in a tangential plane at 1 mm distance from the bell edge. As shown in Fig. 9 (b), the resulting droplet size distribution was compared with measurements using the Malvern Spraytec. The corresponding median sizes D_{v50} are 18.9 μm for the simulation and 17.9 μm for the measurement, which is in quite good agreement. However, inspecting the simulation result in more detail, a certain underrepresentation of larger droplets above 35 μm can be observed. To some extent, this corresponds to the missing large ligaments at the bell edge that will most likely disintegrate into larger droplets. According to experimental studies of high-speed rotary bell atomization carried out by Oswald et al. (2019), film fluctuations that are mainly triggered by the flow around the fastening bolts of the distributor disk on the bell plate may generate film disturbances leading occasionally to the formation of very large drops. Similar results with respect to the influence of the bolts on the film flow were also obtained in the VOF simulations and experiments by Shen et al. (2019).

5.2. Simulations with electric field

The conditions that have been chosen for the simulations with applied electric field are summarized in Table 1. Purposely, the target distance has been fixed at 150 mm since the effect of the electric field strength can be equivalently achieved by different electric voltages. To successfully apply the developed model, the unknown model constant C in (3.9) was determined for each investigated liquid by comparing the measured and the simulated total current using a single set of operating parameters, i.e. an electric potential of 60 kV and a liquid flow rate of 200 ml/min. The obtained model constant C is 13 for the liquid Ba2per and 35 for the paint. Based on Eq. (3.9), the apparent liquid ion mobility can be obtained from the simulations, which, clearly depends on the operating parameter. Detailed results will be shown below.

Simulations were carried out with high voltages of 30, 60 and 80 kV applied to the bell. Fig. 10 shows the velocity contours and the electric potential in the cross-section y = 0 (mid-plane) at 60 kV. For the bell speed of 40 000 1/min the maximum bell velocity at the edge of the 65 mm bell is 136 m s^{-1}. The charge density distribution in the liquid film on the bell surface is shown in Fig. 11(a) for the liquid Ba2per, where the film thickness is between 4 and 6 μm. Similar charge density contours are also observed for the paint liquid, however, at typical film thickness around 14 μm. Basically, higher charge densities are located at the interface between liquid and air, which is expected from classic theory. The maximum charge densities are found close to the bell edge corners, corresponding to the maximum electric field strength in these regions. We can estimate the ion drift velocity $v = k^{*}E$ near the bell wall as $2\times10^{-5} \times 4\times10^{6} = 80$ m s^{-1}, which is much higher than the liquid velocity (~ 2 m s^{-1}) along the bell wall. Consequently, the electric convection due to ion drift velocity plays an important role for the charge migration within the film on the bell.

A clearer picture of the charge distribution inside the wall film for the paint is obtained by plotting the charge density (Fig. 12 (a)) and the charge flux (Fig. 12 (b)) as a function of the distance from the bell surface. The chosen location is indicated in Fig. 12 (a). At this location, the calculated film thicknesses are approximately 15 μm for 200 ml/min and 17 μm for 400 ml/min, keeping in mind that the local grid size is just

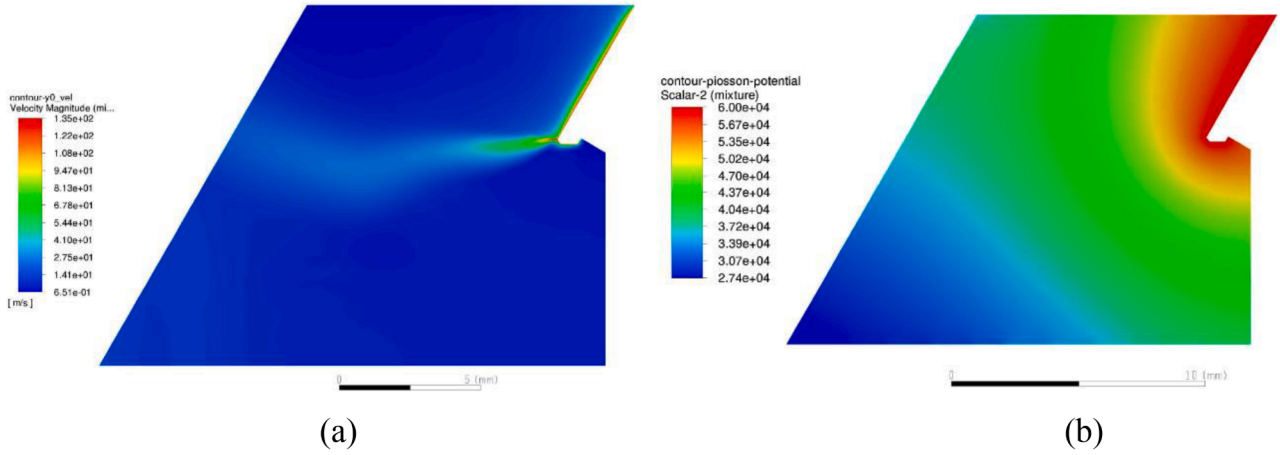


Fig. 10. Air velocity contours m s^{-1} (a) and electric potential V (b) at the cross section y = 0 for Ba2per.

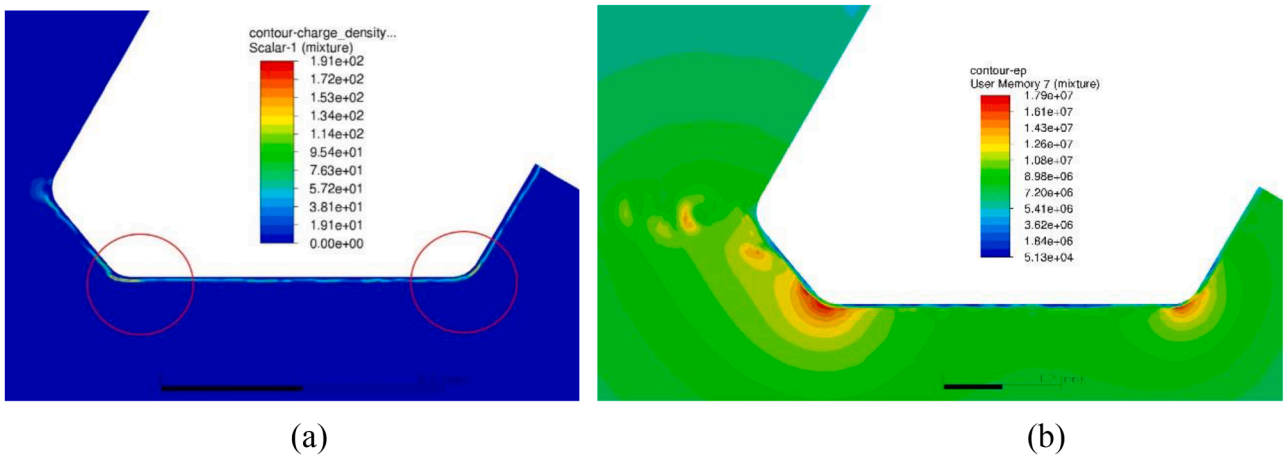


Fig. 11. Distribution of the charge density C/m^3 (a) and the electric field strength V/m (b) at the cross section y = 0 for Ba2per at 200 ml/min flow rate and 60 kV potential.

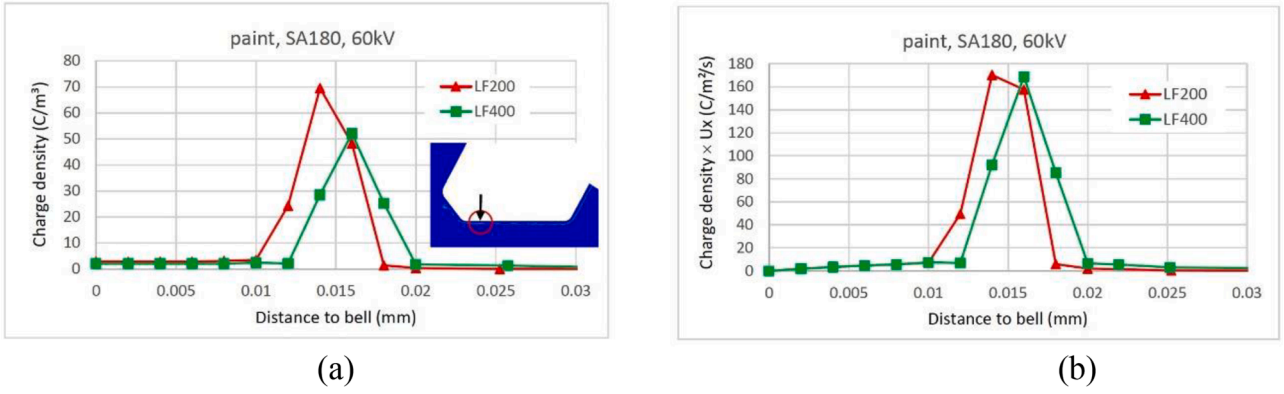


Fig. 12. Distributions across the film at line position: (a) charge density C/m^3, (b): charge flux: $q \cdot u_x$ $C/m^2/s$.

2 μm. Nevertheless, it is evident that the charge is concentrated in a narrow region close to the film surface. Integrating the local charge densities, total charge densities can be estimated, leading to the interesting result of a 27 % higher total charge density in case of 200 ml/min flow rate. By further multiplying the local charge densities by the calculated local radial velocities, charge flux distributions can be derived which are shown in Fig. 12 (b). Here, the ratio of the integration values, which are proportional to the total currents at this location, has diminished to 0.97. The corresponding value for Ba2per is 1,07 and confirms the observation that the total currents are almost independent of the liquid flow rate. However, it should be kept in mind that these results are local. Between the observation location and the detachment point additional charges may migrate into the film.

In Fig. 13, the resulting ligament charges of the two liquids at a flow rate of 400 ml/min and a voltage of 60 kV are qualitatively compared. Obviously, the Ba2per film flows undisturbed over the first sharp edge of

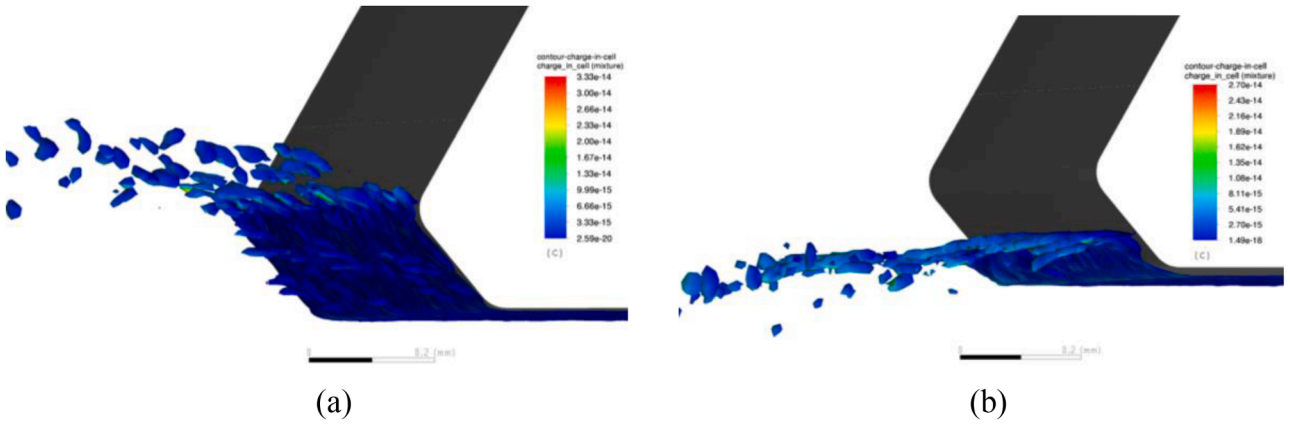


Fig. 13. Electric charge (C) on liquid ligaments with the liquid flow rate of 400 ml/min and a voltage of 60 kV, (a): Ba2per with a shaping air flow rate of 50 sl/min, (b): paint with a shaping air flow rate of 180 sl/min.

the bell surface, finally detaching at the upper sharp edge. This is mainly because of the relative low shaping air flow rate of 50 sl/min and partly because of the lower viscosity. In contrast, the paint film at 180 sl/min shaping air detaches already at the first edge. Close to the detachment point, simulation results show that the radial velocity of the lumps is around 10 - 30 m s^{-1}, which means that the charge migration is affected significantly by the flow convection also.

After breakup, the total currents can be calculated by collecting all droplets that move through the inspection plane. Simulated and experimentally obtained currents are compared in Fig. 14. In general, a quite good agreement can be observed. As expected, the current increases with increasing electric field strength that can be realized by increasing the applied electric potential (as shown here) or by decreasing the distance between bell and grounded target. The water-based paint carries more charge than the liquid Ba2per because of the higher electric conductivity of the paint. Especially in the case of paint, there is a nice agreement between experiment and simulation with respect to the limited influence of the liquid flow rate on the total current. The biggest difference between experimental and simulated results, which is about 20 %, occurs for Ba2per at a flow rate of 400 ml/min.

Furthermore, the obtained individual droplet charges were evaluated in more detail. As an example, the obtained results in case of Ba2per at an applied potential of 60 kV and a flow rate of 200 ml/min are shown in Fig. 15. In general, the droplet charge increases with droplet diameter. By neglecting the small droplet fraction, namely droplets below 2 μm, the fitting curve (Fig. 15 a) shows a proportional relationship of charge to $d^{3.1}$, i.e. very close to the droplet volume, which is in contrast to the Rayleigh-limit (Rayleigh, 1882) ($Q \propto d^{3/2}$). This behaviour is common for all simulations, i.e. for both liquids and the respective parameters. For droplets larger than approximately 6 μm, a constant charge density (Fig. 15 b) can be observed. Finally, the droplet charges can be analysed with respect to the Rayleigh-limit that defines the surface charge required to cause breakup of a charged droplet. Fig. 15 c) shows the ratio between the droplet charge and the corresponding Rayleigh charge limit. It can be observed that in case of the Ba2per this ratio increases with increasing droplet diameter. Droplets with diameters around 20 μm, which represent the strongest fraction of the size distribution, are charged to about 5% of the corresponding Rayleigh limit. For the paint with corresponding parameters we obtained a similar correlation but with $Q/Q_{Ray} \approx 0.08$ for the 20 μm droplet range. It is interesting to note that similar fractions of the Rayleigh limit were also used as empirical assumptions for the droplet charges in old simulations of the spray coating (Domnick et al., 2005; Viti et al., 2010; Guettler et al., 2020), however, a constant ratio of Q/Q_{Ray} was applied for all droplet classes, which is quite different from the present results.

The spray formation, namely the distribution of the droplets close to the bell are depicted in Fig. 16 (a) and Fig. 17 (a). In the two cases, Ba2per at very low shaping air flow rate and paint at higher shaping air flow rate, a significant influence of the applied potential on the initial droplet propagation direction is observed. With applied potential, the resulting electric forces tend to accelerate the droplets in the direction of the grounded target. This effect might be supported by the change of the detachment line moving downward if potential is applied. To characterize the initial droplet velocities in more detail, a tangential observation plane with a distance of 1 mm from the bell edge (see black line in Fig. 16 (a)) has been defined. The obtained axial droplet velocity components u_z as a function of the droplet diameter are shown in Figs. 16 (b) and 17 (b). Positive velocity values denote velocities in target direction.

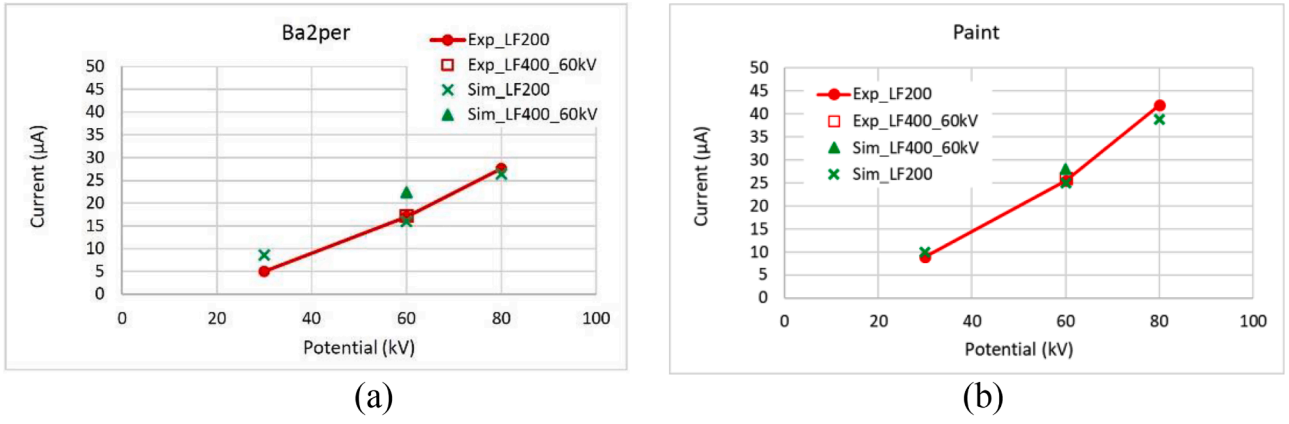


Fig. 14. Effect of the electric potential and the liquid flow rate on the target current, (a): Ba2per, (b): paint.

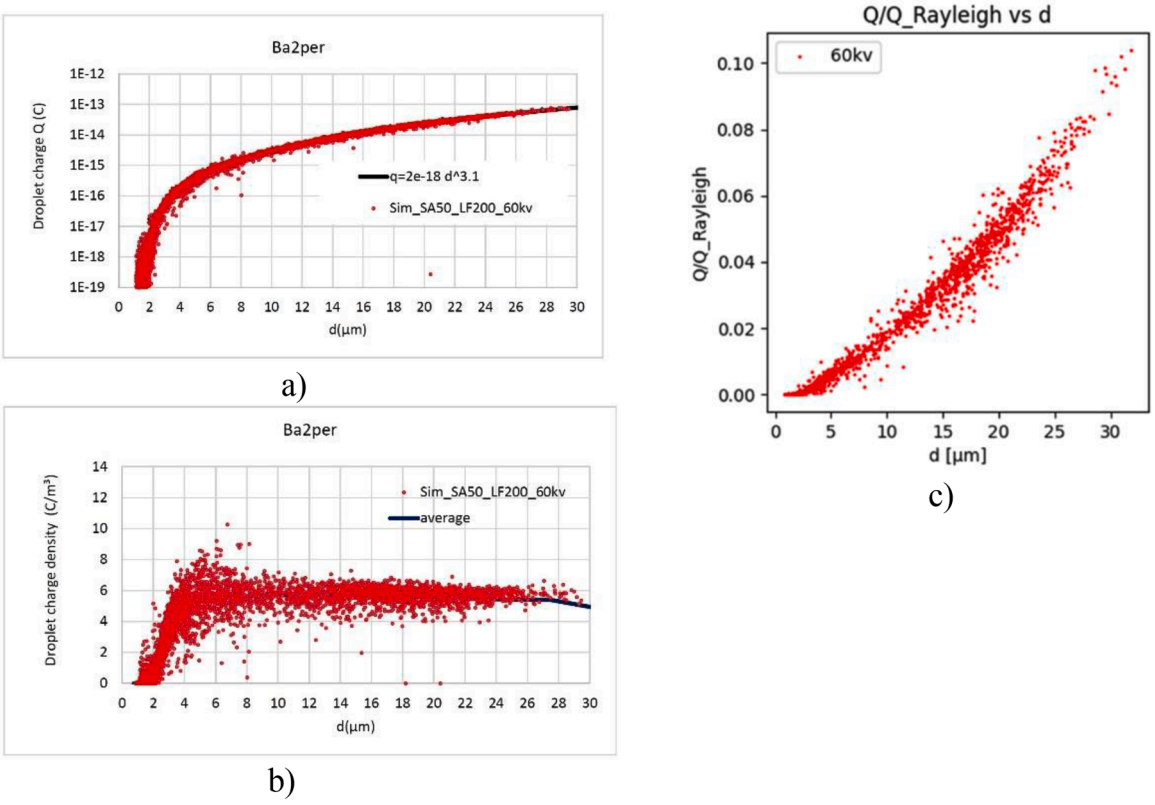


Fig. 15. (a): Droplet charge distribution C, (b): Droplet charge density C/m^3, (c): Ratio between droplet charge and Rayleigh limit for Ba2per.

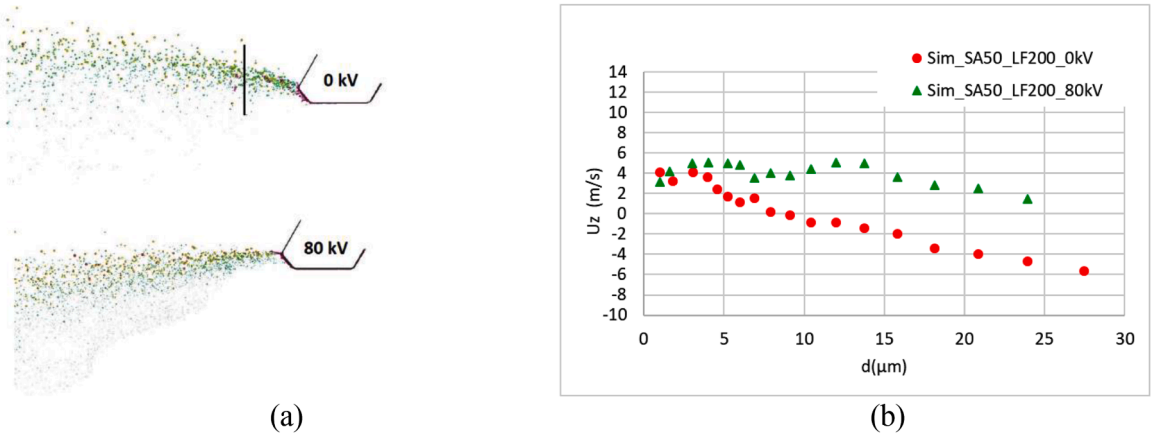


Fig. 16. (a): Spray structure for Ba2per with the operating parameters SA = 50 sl/min, n = 40 000 1/min, LF = 200 ml/min. (b): The corresponding initial droplet velocity u_z in bell axis direction; a black line shows the position of the collecting plane for the droplet analysis.

The obtained qualitative change in the spray direction is consistently indicated by the velocities. In both cases, the axial velocity components increase with applied potential. Interestingly, in case of Ba2per with low shaping air and without potential, the initial velocities of droplets larger than approximately 8 µm are negative, i.e. the droplets move in backward direction. Clearly, this operating condition leads to a spray flow that is fully outside any practical relevance, as it would inevitably produce severe pollution of atomizer or robot parts. Considering the cases Ba2per at 80 kV and paint (high shaping air) at 0 kV this situation has improved, but the initial spray direction is still mainly radially orientated. In case of paint at 80 kV, however the major droplet propagation is directed downward towards the target, which together with the effect of the shaping air results in a reasonably confined spray cone between atomizer and target. It should be noted that these results are also essential to improve the quality of necessary inlet conditions for full scale simulations of the painting process, aiming to estimate film thickness distributions on the target and transfer efficiencies.

Droplet mean diameters were also analysed. As already discussed in Section 2, the volume weighted mean diameter D_{30} was used to compare experimental and numerical results. As indicated by Fig. 18 a) for the Ba2per case, a quite good agreement between the experiment (PDA) and the simulation can be observed for the electric voltages smaller than 60 kV. With increasing electric field, the droplet mean diameter decreases slightly, which is consistent to some numerical investigations (Pendar and Páscoa, 2021; Krisshna et al., 2023) considering high-speed rotary bells. By significantly increasing the applied electric potential up to 80kV, the reduced mean diameter D_{30} of the simulations indicates a rising production of smaller droplets. As we have pointed out in Section

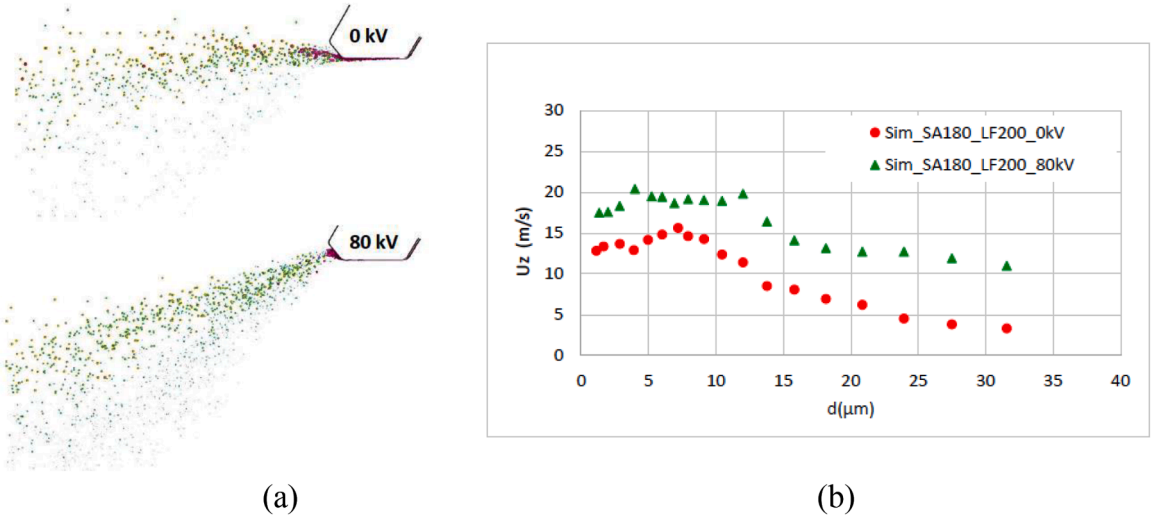


Fig. 17. (a): Spray structure for paint with the operating parameters SA = 180 sl/min, n = 40 000 1/min, LF = 200 ml/min. (b): The corresponding initial droplet velocity u_z in bell axis direction.

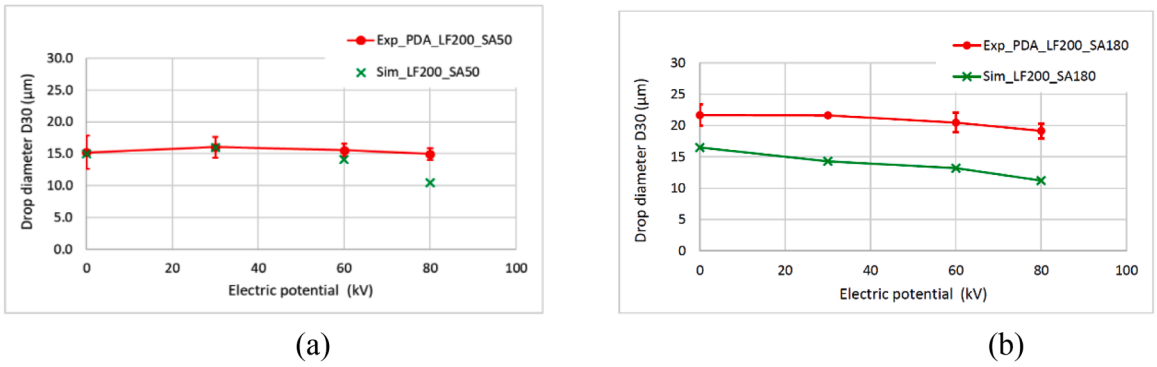


Fig. 18. Comparison of droplet mean diameter $D_{30,}$ (a): Ba2per (n = 40 000 1/min, LF = 200 ml/min and SA = 50 sl/min), (b): paint (n = 40 000 1/min, LF = 200 ml/min and SA = 180 sl/min).

2, the PDA system could not detect reliably quite small droplets, which may explain the relatively large difference between the simulated and measured D_{30} for Newtonian liquid Ba2per at this condition. For water-based paint liquid, a significant difference over the whole investigated potential range is observed between the measured and the simulated mean droplet diameter. Probably, the viscosity model applied in the simulation is too simple. It is well known that water-based paints do not only show the considered shear thinning behaviour, but have also thixotropic and elongational viscosity effects (Seeler et al., 2017; Oswald et al., 2018), that are not accounted for. Therefore, in further numerical studies, a more complex rheological model should be considered.

Finally, we would like to discuss the effect of the proposed apparent ion mobility concept on the simulation results of charge injection and migration, which is an extension to other research work (van Poppel et al., 2010; Krisshna et al., 2023) mostly applying a constant ion mobility. For a given liquid, the dominant parameter in (3.9), defining the apparent ion mobility, is the electric field in the film on the bell surface. However, as shown by Fig. 11 (b), the electric field strength depends on the local bell position. Therefore, the apparent ion mobility is a function of the position. Consequently, a mean apparent ion mobility was calculated and applied in the solution of the charge conservation equation. The corresponding values are shown in Fig. 19. The ion mobility decreases with increasing electric field. To understand this phenomenon, the charge Eq. (3.8) should be considered in more detail.

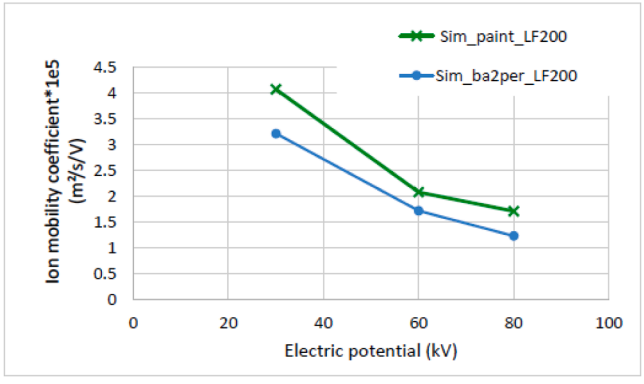


Fig. 19. Effect of electric potential on the apparent ion mobility coefficient (liquid flow rate LF = 200 ml/min).

Here, a reduced negative source term $-k\frac{q^2}{\varepsilon}$ will result in a higher charge in the liquid film, corresponding to a lower apparent ion mobility for the case of higher electric potential. A consistent consideration can be performed with respect to the influence of the two liquids, differing not only in electric conductivity and permittivity, but also in the film thickness and the electric field on the bell.

Fig. 19 indicates a higher ion mobility coefficient of the paint

compared to Ba2per. Despite the higher apparent ion mobility of the paint material, its higher relative permittivity strongly reduces the negative source term, resulting finally in a higher target current. A similar analysis can also be made with respect to the effect of the liquid flow rate on the target current. For a given liquid, a higher liquid flow rate results in a thicker film on the bell surface, leading to a higher apparent ion mobility and negative source term, consequently creating lower charges in the thicker liquid film as already indicated in Fig. 12.

There are only a few studies of the effect of strong electric fields on the ion mobility in leaky dielectric liquids. In our case, we successfully applied what we call apparent ion mobility approach to explain our simulation and experimental results based on the solution of the conservation equations. Nevertheless, there are still remaining questions, e.g. why the ion mobility decreases with increasing electric field strength. A possible explanation might be the presence of strong inherent ion interactions leading to reduced ion drift velocities. In any case further studies on this aspect should be carried out.

In the present numerical study, we included the diffusion term in the transport Eq. (3.8) of the charge density. The magnitude distributions of the source term and the diffusion term in liquid film on the bell wall were analysed and compared for a given case with the rather high conductive water borne paint material. Near the bell edge the source term is about ten times larger than the diffusion term, but in other positions only 1-2 times. More detailed investigation, especially for paints with lower conductivity should be carried out in future.

6. Conclusions

This paper presents experimental and simulation studies on the liquid atomization process of a high-speed rotary bell with an internal charging system, focussing on the investigation of the effects of electrohydrodynamics on charging behaviour and on liquid breakup. For such a kind of atomizer, it is the first investigation including the simulation of charge migration from the electrode, i.e. the bell surface, to the liquid film and to the forming droplets. As model liquids, a Newtonian liquid and a water-based paint were applied.

The commercial CFD code ANSYS Fluent with user-defined scalar transport equations solving the electric field and the charge density was applied to study the interaction of the fluid with the electric field. We solved the charge conservation equation for leaky dielectric liquids proposing an apparent ion mobility model. It was found that the electric convection plays an important role for the charge migration in the liquid film on the bell. The charge distribution was inhomogeneous in the film on the bell, with the charge mainly accumulating at the liquid-air film interface. For the liquid ligaments that detach from the bell wall, the effect of fluid convection on the charge transport cannot be neglected since the detaching ligaments are strongly accelerated by the effect of the high tangential velocity. Simulated droplets size distributions and charge distributions were also analysed with the mean droplet diameters being partly in good agreement with experimental results. It was found that the effect of electric field on the liquid breakup is weak, but nevertheless noticeable. In case of paint, existing differences between experiments and simulations might be due to a simplified rheological model.

The simulated total currents, calculated by the summation of the individual droplet charges, were found to be in a reasonably good agreement with experimental results. Based on the simulation results, we could further explain some experimental results that were not expected, such as the only minor effect of the liquid flow rate on the target current. In addition, the simulation results indicate that the droplet charge is mainly proportional to d^3, i.e. the droplet volume.

The apparent ion mobility model used in this study indicated interesting results, e.g., that in presence of strong electric fields the ion mobility cannot be a constant but decreases with increasing electric field strength. Further studies are required to investigate these effects in more detail.

Based on these results and the additional information on the droplets quite close to the bell, namely diameter, velocity and position, we are able to perform improved calculations of the whole spray propagation, the resulting film thickness distribution on the target and the transfer efficiency in industrially relevant painting applications.

CRediT authorship contribution statement

Q. Ye: Writing – review & editing, Writing – original draft, Investigation. **B. Shen:** Writing – original draft, Validation, Investigation. **O. Tiedje:** Writing – review & editing, Project administration, Investigation. **P. Knee:** Visualization, Investigation. **J. Domnick:** Writing – review & editing, Writing – original draft, Investigation.

Declaration of competing interest

The authors declare that they have no known competing financial interests or personal relationships that could have appeared to influence the work reported in this paper.

Data availability

Data will be made available on request.

Acknowledgements

The present investigations were funded by the Bundesministerium für Wirtschaft und Klimaschutz under the support of the AiF *Arbeitsgemeinschaft industrieller Forschungsvereinigungen* (IGF-project number 21873 N) and the Deutschen Forschungsgesellschaft für Oberflächenbehandlung e.V. The work has been also supported by the High-Performance Computing Center (HLRS) in Stuttgart (German federal project: PbusRobe).

References

Aramide, B., Kothandaraman, A., Edirisinghe, M., Jayasinghe, S.N., Ventikos, Y., 2019. General computational methodology for modeling electrohydrodynamic flows: prediction and optimization capability for the generation of bubbles and fibers. Langmuir 35, 10203–10212.

Bandara, T., Mellander, B.E., 2011. Evaluation of mobility, diffusion coefficient and density of charge carriers in ionic liquids and novel electrolytes based on a new model for dielectric response. In: Kokorin, A. (Ed.), Ionic Liquids: Theory, Properties, New Approaches. IntechOpen, London.

Bayvel, L.P., Orzechowski, Z., 2018. Liquid Atomization. Routledge, Boca Raton.

Castellanos, A., 1998. Electrohydrodynamics: Outcome of a Series of Lectures Delivered at the Seventh IUTAM (International Union of Theoretical and Applied Mechanics) summer School Held in Udine, Italy in July 1996. Springer, Wien, p. 363.

Chen, Y., Chen, W., Li, B., Zhang, G., Zhang, W., 2017. Paint thickness simulation for painting robot trajectory planning: a review. Ind. Robot 44, 629–638.

Clark, R., von Domaros, M., McIntosh, A.J.S., Luzar, A., Kirchner, B., Welton, T., 2019. Effect of an external electric field on the dynamics and intramolecular structures of ions in an ionic liquid. J. Chem. Phys. 151, 164503.

Crowe, C.T., Schwarzkopf, J.D., Sommerfeld, M., Tsuji, Y., 2011. Multiphase Flows with Droplets and Particles. CRC Press.

Domnick, J., Scheibe, A., Ye, Q., 2005. The simulation of the electrostatic spray painting process with high-speed rotary bell atomizers. Part I: Direct charging. Part. Part. Syst. Charact. 22, 141–150.

Guettler, N., Knee, P., Ye, Q., Tiedje, O., 2020. Initial droplet conditions in numerical spray painting by electrostatic rotary bell sprayers. J. Coat. Technol. Res. 17, 1091–1104.

Gzowski, O., 1962. Mobility of ions in liquid dielectrics. Nature 194, 173.

Hartman, R., Brunner, D.J., Camelot, D., Marijnissen, J., Scarlett, B., 1999. Electrohydrodynamic atomization in the cone–jet mode physical modeling of the liquid cone and jet. J. Aerosol. Sci. 30, 823–849.

Hinze, J.O., Milborn, H., 1950. Atomization of liquids by means of a rotating cup. J. Appl. Mech. 145–153.

Kourmatzis, A., Shrimpton, J.S., 2009. Electrohydrodynamics and charge injection atomizers: a review of the governing equations and turbulence. At. Sprays 19, 1045–1063.

Krisshna, V., Liu, W., Owkes, M., 2023. High-fidelity simulations of a rotary bell atomizer with electrohydrodynamic effects. Int. J. Multiph. Flow 168, 104566.

Lastow, O., Balachandran, W., 2006. Numerical simulation of electrohydrodynamic (EHD) atomization. J. Electrostat. 64, 850–859.

Liu, D., Liu, Q., Liu, B., Wang, Z., 2020. Modelling the electrostrictive-force induced cavitation formation process in dielectric liquids. In: Proceedings of the 7th IEEE International Conference on High Voltage Engineering and Application. ICHVE 2020, September 6-10. Beijing, China, Piscataway, NJ. IEEE, pp. 1–4.

Mark, A., Andersson, B., Tafuri, S., Engstrom, K., Sorod, H., Edelvik, F., Carlson, J.S., 2013. Simulation of electrostatic rotary bell spray painting in automotive paint shops. At. Sprays 23, 25–45.

McCarthy, J.J.E., Senser, D.W., 2006. Numerical model of paint transfer and deposition in electrostatic air sprays. At. Sprays 16, 195–222.

Melcher, J.R., 1981. Continuum Electromechanics. MIT Press, Cambridge, Mass, Getr. Zählung.

Oswald, W., Goedecke, L., Ehrhard, P., Willenbacher, N., 2018. Effect of elongational flow behavior on ligament disintegration and drop formation by mean of a high-speed rotary bell atomizer. In: Proceedings of the 14th Triennial International Conference on Liquid Atomization and Spray Systems July 22-26. Chicago, IL, USA.

Oswald, W., Lauk, J., Gödeke, L., Ehrhard, P., Willenbacher, N., 2019. Analysis of paint flow pulsations during high-speed rotary bell atomization. Coatings 9, 674.

Ouedraogo, Y., Gjonaj, E., Gersem, H., Steinhausen, C., Lamanna, G., Weigand, B., 2021. Simulation and characterization of transient and steady state electrosprays. ICLASS 2021. https://doi.org/10.2218/iclass.2021.6034.

Pendar, M.R., Páscoa, J.C., 2021. Numerical analysis of charged droplets size distribution in the electrostatic coating process: effect of different operational conditions. Phys. Fluids 33.

Rayleigh, L., 1882. On the equilibrium of liquid conducting masses charged with electricity. Lond. Edinb. Dublin Philos. Mag. J. Sci. 14, 184–186.

Seeler, F., Hager, C., Tiedje, O., Schneider, M., 2017. Simulations and experimental investigation of paint film leveling. J. Coat. Technol. Res. 14, 767–781.

Shen, B., Ye, Q., Guettler, N., Tiedje, O., Domnick, J., 2019. Primary breakup of a non-Newtonian liquid using a high-speed rotary bell atomizer for spray-painting processes. J. Coat. Technol. Res. 16, 1581–1596.

Stevenin, C., Béreaux, Y., Charmeau, J.Y., Balcaen, J., 2015. Shaping air flow characteristics of a high-speed rotary-bell sprayer for automotive painting processes. J. Fluids Eng. 137.

Thieme, M., Domnick, J., 2006. Atomization characteristics of high-speed rotary bell atomizers. At. Sprays 16, 857–874.

van Poppel, B.P., Desjardins, O., Daily, J.W., 2010. A ghost fluid, level set methodology for simulating multiphase electrohydrodynamic flows with application to liquid fuel injection. J. Comput. Phys. 229, 7977–7996.

Viti, V., Kulkarni, J., Watve, A., 2010. Computational fluid dynamics analysis of the electrostatic spray painting process with a rotating bell cup. At. Sprays 20, 1–17.

Wilson, J., Grib, S., Darwish Ahmad, A., Renfro, M., Adams, S., Salaimeh, A., 2018. Study of near-cup droplet breakup of an automotive electrostatic rotary bell (ESRB) atomizer using high-speed shadowgraph imaging. Coatings 8, 174.

Zhou, L., 2023. A review for measurements and simulations of swirling gas-particle flows. Exp. Comput. Multiph. Flow 5, 133–141.